

# Structural density of dendritic microstructures grown in circular domains: Micro- and nano-scale investigation

Cite as: Phys. Fluids **37**, 052104 (2025); doi: 10.1063/5.0267533

Submitted: 24 February 2025 · Accepted: 18 April 2025 ·

Published Online: 9 May 2025



View Online



Export Citation



CrossMark

Asghar Aryanfar,<sup>1,a)</sup> Trina Dhara,<sup>2,3</sup> and Sunando DasGupta<sup>2</sup>

## AFFILIATIONS

<sup>1</sup>Boğaziçi University, Bebek, Istanbul 34342, Turkey

<sup>2</sup>Indian Institute of Technology Kharagpur, West Bengal 721302, India

<sup>3</sup>Cornell University, 113 Ho Plaza, Ithaca, New York 14853, USA

<sup>a)</sup> Author to whom correspondence should be addressed: [aryanfar@caltech.edu](mailto:aryanfar@caltech.edu)

## ABSTRACT

The stochastic instigation and growth of needle-like microstructures during the charging period in the rechargeable batteries can cause hazard and short circuit during the utilization, such that they control the state of health and longevity. Herein, we aim at establishing the relationship between the solid-mass/empty-space fractions of the growing electrodeposits and elaborate on the interrelation of such structural density with the electrodeposition parameters. We initially tackle on estimating the micro-scale density  $\rho_{\text{Micro}}$  behavior through percolation-based image processing of the copper electrodeposition experiments and correlate them to the bulk salt concentration  $C_0$  as well as the applied voltage  $V_0$ . Subsequently, we establish a theoretical model for the growth rate of microstructures, considering both micro- and nano-scale porosity. Since the porosity of the growing microstructures directly correlates with their kinetics (i.e., rate) of growth, we have estimated the nano-scale density on the order of  $\rho_{\text{Nano}} \sim [10^{-4}, 10^{-3}]$  via comparing the rate of porous ramification in the experiments and modeling frameworks. Consequently, we address the branching pattern of the dendritic microstructures and compute their real-time fractal dimension vs the applied voltage as well as the concentration and explain it in terms of oscillatory behavior between the nucleation and the branching. The obtained understanding from the correlation of density with the concentration and applied voltage, as well as the inherent atomic-scale density range in the amorphous electrodeposits, could help to tune the morphology of the electrodeposits, which could be helpful in applications such as rechargeable batteries to avoid short circuit and enhance longevity.

Published under an exclusive license by AIP Publishing. <https://doi.org/10.1063/5.0267533>

## I. INTRODUCTION

Electrodeposition has long been investigated as a key electrochemical process, utilized, and observed in a wide variety of applications such as electroplating<sup>1,2</sup> and e-coating,<sup>3,4</sup> with particular implications in electrochemical devices such as rechargeable batteries,<sup>5</sup> fuel cells,<sup>6</sup> and semiconductor industry.<sup>7</sup> Battery-wise, the recent approaches for utilization of high-energy density metal electrodes, which lack the intercalation mechanism of the conventional graphite, emphasize further the significance of the electrodeposition,<sup>8</sup> which requires efficient morphological engineering for the electrodeposited active material.<sup>9</sup>

The suppression of the so-called dendritic metallic microstructures has been challenging for various metal based batteries.<sup>10,11</sup> In particular, the enormous structural variation such as needle-like, mossy, and fractal morphology of deposits over the prolonged

charge–discharge cycles has emerged as a critical concern.<sup>12,13</sup> In this regard, the solid density or porosity of the growing electrodeposits has been a key parameter, since the inclusion of the voids inflates the microstructure to a large extent, such that it can pass through the separator's pores and cause disastrous short-circuit.<sup>14</sup> Furthermore, the loosely packed porous microstructures are prone to be dissociated from the so-called necks as the most vulnerable portions, leading to the Coulombic loss as well as thermal instability.<sup>15</sup> Therefore, intensive research is being conducted to control electrodeposition morphology by modulating electrolyte composition,<sup>16–18</sup> electrode architecture,<sup>19,20</sup> surface-to-volume control by adjusting porosity,<sup>21–24</sup> charging strategy,<sup>25–28</sup> utilization of laser for engineering the coating in smaller scales,<sup>19,29</sup> and altering the super-hydrophobicity.<sup>30</sup> Meanwhile, the temperature as an externally controlled and non-invasive parameter has been quantified<sup>31</sup> and utilized as a constant value<sup>32,33</sup> and gradient form,<sup>34,35</sup> in particular, in

analogy with the solidification process.<sup>36</sup> Nonetheless, the grown electrochemical microstructures have been proposed to have a certain degree of fractality.<sup>37,38</sup>

Modeling-wise, previous frameworks for the dendritic electrodeposition emphasized the space charge region<sup>39</sup> and the role of electric fields, whereas others correlated the prominent growth drive to the diffusion limited aggregation (DLA).<sup>40,41</sup> Meanwhile, electrodeposition in radial form has gotten remarkable attention for explaining the morphological features,<sup>42</sup> where the fractal tendency and density have been explored in terms of the applied voltage and involved concentration<sup>38,43,44</sup> as well as the interface curvature.<sup>45</sup>

In the previous study, the dynamics (i.e., rate) of dendritic propagation was correlated with the distribution of the electric field within the circular domain, for the range of parameters considered, which was obtained via tracking the microstructure reach in time.<sup>46</sup> Herein, we address the structural aspects of the microstructures and their correlation with the involved parameters such as the electrolyte concentration  $C$  and the applied voltage  $V$ . Establishing a percolation-based framework, we initially define density forms in micro-scale ( $\rho_{\text{Micro}}$ ) for the microstructures, which is the solid fraction that can be computed from the experimental images down to the resolution of a single pixel, and compute their transition vs the growth life of the evolving microstructures. Furthermore, for estimating the range of lower-scale density, which extend into the atoms, we develop a new model to anticipate the rate of the propagation  $v$  of the advancing electrodeposit front, with the presumed density  $\rho$ . Correlating the experimental and computational rates of propagation, we get an estimation for the nano-scale density  $\rho_{\text{Nano}}$  of the growing microstructures, which could not get captured in the experimental measurements. Consequently, the transition in the fractal dimension of the growing structures supplements the underlying insights behind the oscillatory pattern in the morphological evolution. The obtained framework could be useful for optimizing the space of parameters for controlling and efficient compression of the electrochemical deposits.

## II. EXPERIMENTAL

The experiments were performed in an established rounded electrochemical cell, as illustrated in Fig. 1. The copper wires (AWG 28,  $0.2 \Omega \text{ m}^{-1}$ ,  $d = 0.321 \text{ mm}$ ) were purchased from Khaitan Winding Wire Pvt. Ltd. (KWW Wires and Strips), and they were polished using a sand paper of grit 200 and were bent into a circular shape ( $d_0 = 18 \text{ mm}$ ) for utilization as anode. Subsequently, it was locked on a microscopic glass slide which was provided from HiMedia Laboratories Pvt. Ltd. Conversely, for cathode, the tip of a copper wire (AWG 32,  $\rho = 0.5 \Omega \text{ m}^{-1}$ ,  $d_l = 0.202 \text{ mm}$ ), acquired from KWW Wires and Strips, was placed manually at the center of the circular counter-electrode. The entire domain was filled with the electrolyte solution drop by drop using a micropipette, that is, the specified concentrations of copper sulfate salt ( $\text{CuSO}_4 \cdot 5\text{H}_2\text{O}$ , EMPLURA 99%) in de-ionized water (Milli-Q, 99.8%). The ends of the electrodes were connected to the power source (KEITHLEY 2410 1100 V Source-meter), and the array of the specified voltage  $V_0$  was applied in separate experiments. A camera with macro-lens is fixed below the glass slide to capture the microstructure evolution from the bottom. During each individual experiment, the microstructures initiated from the inner electrode (i.e.,  $d_l$ ) and progressively propagated toward the counter-electrode (i.e.,  $d_0$ ). The range of variation in the applied

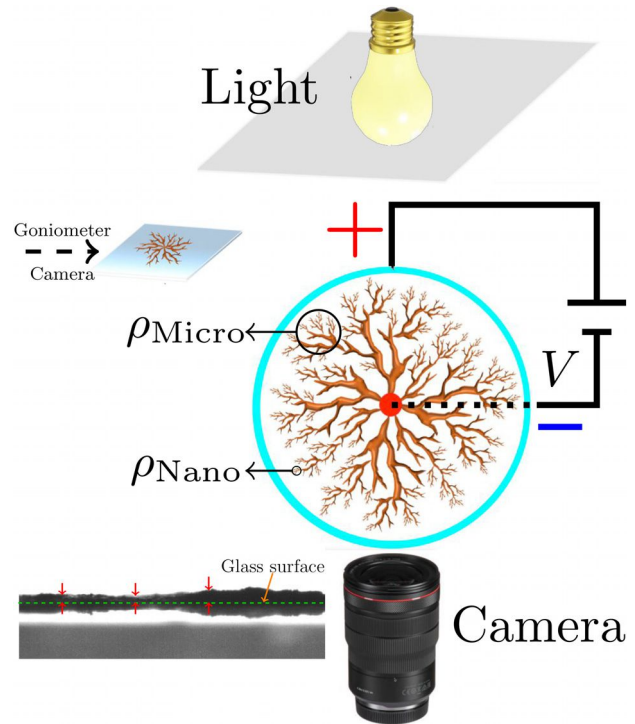


**FIG. 1.** Schematics for experimental observation and tracking the growing microstructures. The circular propagation occurs when imposing the voltage  $V$  through the circuit which deposits the ions from the larger ring electrode (cyan) into the smaller electrode at the center (red). As the result, the electrodeposits grow from center toward the periphery. The sample zones for larger  $\rho_{\text{Micro}}$  and smaller  $\rho_{\text{Nano}}$  scale densities are illustrated. The inset images on the left top present the schematics for post-experiment measurement for the thickness, from the lateral view, using a goniometer, and the left bottom image presents the sample thickness measurements from different positions of the microstructure.

voltage  $V_0$ , the electrolyte concentration  $C_0$ , and the image acquisition rate are summarized in Table I.

The range of the voltage  $V_0$  and concentration  $C_0$  were chosen such that the electrolyte would not dry out during the prolonged time requirement (occurring for smaller voltages  $V_0$ ) till short-circuiting and there is noticeable variation in the obtained morphologies, particularly where the internal pores become the most visible. After each experiment, the wire electrode was disconnected, and the electrolyte solution and the anode electrode were removed cautiously so as not to distort the microstructure. Subsequently, the electrolyte solution was removed carefully, the remaining was dried, and the side view of the structure sitting on the glass slide was captured using a goniometer

**TABLE I.** Experimental parameters. The electrodes are copper  $\text{Cu}$ , and the electrolyte is aqueous copper sulfate  $\text{CuSO}_4$  solution (i.e.,  $C_0$ ).

$d_l$ (mm)	$d_0$ (mm)	$V_0$ (V)	$C_0$ (mM)	Acquisition rates (Frame $\text{s}^{-1}$ )
0.2	18	{3, 4, 5, 6, 7}	{5, 10, 25}	{ $\frac{1}{20}$ , $\frac{1}{30}$ , $\frac{1}{40}$ }

(Dataphysics OCA 15Pro), leading to the mean thickness of the microstructures as  $\bar{b} \approx 30 \mu\text{m}$ , as shown in Fig. 1, left insets.

Figures 2(a) and 2(b) illustrate two classes of morphologies with branches and packed structures for specific values of the applied voltage  $V_0$ , the electrolyte concentration  $C_0$ , and the time span  $t$ .

### III. COMPUTATIONAL

In order to capture the larger scale pores discernible in the optical images, we perform image processing. The acquired experimental images possess a certain resolution, where the pixel-level scale controls the limit for discerning the microstructure from the empty space. Each individual pixel in the images can be estimated as below:

$$\beta = \frac{\text{Image Size}}{\text{Number of pixels}} = \frac{18 \times 10^{-3} \text{m}}{1500 \text{pixels}} \approx 12 \mu\text{m}/\text{pixel}, \quad (1)$$

where  $\beta$  is the calibration factor between the image pixel and the reality. Hence, the density measurement in an image can be counted on the order of  $12 \mu\text{m}$  which is termed as  $\rho_{\text{Micro}}$ . On the other hand, the emptiness inside the observed structure, that is, beyond the limit of the current experimental window, can be extended down to atomic level and comprehended as the smaller scale density of the microstructure, termed as  $\rho_{\text{Nano}}$ . In fact, the total density  $\rho$  is expressed as follows:

$$\rho = \frac{A_S}{A_{\text{TOT}}}, \quad (2)$$

where  $A_S$  is the area of the solids, and  $A_{\text{TOT}}$  is the total covered area. As well, the micro-density  $\rho_{\text{Micro}}$  can only capture the pores in the larger scale, as

$$\rho_{\text{Micro}} = \frac{A_{\text{Grain}}}{A_{\text{TOT}}},$$

where  $A_{\text{Grain}}$  is the solid-interpreted regions in the image processing, which (might) have extra pores in atomic scale. However, in reality,  $A_{\text{Grain}}$  contains additional pores in smaller (i.e., atomic) scale expressed with  $\rho_{\text{Nano}}$ . Hence,

$$\rho_{\text{Nano}} = \frac{A_S}{A_{\text{Grain}}}.$$

Therefore, by expansion of the total density definition in Eq. (2), one has

$$\begin{aligned} \rho &= \frac{A_{\text{Grain}}}{A_{\text{TOT}}} \times \frac{A_S}{A_{\text{Grain}}} \\ &= \rho_{\text{Nano}} \times \rho_{\text{Micro}} \end{aligned} \quad (3)$$

Hence, the total density  $\rho$  of the microstructure is expressed in terms of two densities in the larger ( $\rho_{\text{Micro}}$ ) and smaller ( $\rho_{\text{Nano}}$ ) scales.



(a) Branched morphology samples formed at  $\{C_0, V_0\} = \{(5, 5, 10) \text{mM}, (4, 5, 5) \text{V}\}$  and times  $t = \{440, 360, 200\} \text{s}$  respectively.



(b) Packed morphology samples formed at  $\{C_0, V_0\} = \{(10, 25, 25) \text{mM}, (6, 6, 6) \text{V}\}$  and times  $t = \{150, 120, 150\} \text{s}$  respectively.

**FIG. 2.** The variation in the observed morphology of the evolved dendritic electrodeposits vs the electrolyte concentration  $C_0$ , the applied voltage  $V_0$ , and the time  $t$ .

Herein, we explain each term and approach computing the density across each scale ( $\rho_{\text{Micro}}, \rho_{\text{Nano}}$ ), as below.

**A. Micro-density  $\rho_{\text{Micro}}$**

The process for computing the micro-density  $\rho_{\text{Micro}}$  involves distinguishing the material zone from the void space via counting the recognized pixels for either media. The steps for processing the acquired images as a function of the applied voltage  $V$ , the electrolyte concentration  $C_0$ , and the time  $t$  are presented as below:

1. Each RGB image contains information about the intensity of the red ( $R$ ), green ( $G$ ), and blue ( $B$ ) colors, in each individual pixel, which by definition spans between 0 (no intensity) and 255 (full intensity), and therefore each pixel contains three distinct values of  $\{R, G, B\} \in [0, 255]$ . After acquiring such information, the color image is transformed into the respective gray-scale intensity image  $Int$  by using the conventional coefficients  $f$  for each color compartment as<sup>47</sup>

$$f = [0.299 \quad 0.587 \quad 0.114],$$

which yields

$$Int = \frac{1}{255}(f_R R + f_G G + f_B B).$$

Obviously, the obtained gray-scale image is normalized version of weighted  $RGB$  image to its maximum value; hence,  $Int_{i,j} \in [0, 1]$ .

2. In order to discern the solid sites (1) from the void regions (0), the image  $Int_{i,j}$  should be binarized. Several thresholding methods have been proposed based on shape,<sup>48</sup> cluster,<sup>49</sup> entropy,<sup>50</sup> attribute-based,<sup>51</sup> and locally adaptive<sup>52</sup> optimization of the gray-scale image. Since the foreground (black) and the background (white) image zones in this study highly distinct, with minimal so-called gray region, the outcome for selecting either thresholding method should be very similar. Herein, we utilize Otsu’s popular method for optimized thresholding.<sup>53</sup> In this regard, the threshold value  $Int_c$  determines if a given pixel will be turned to black (i.e., 0) or white (i.e., 1), as below:<sup>54</sup>

$$J_{ij} = \begin{cases} 1 & Int_{i,j} \geq Int_c \\ 0 & Int_{i,j} < Int_c. \end{cases} \quad (4)$$

The threshold  $Int_c$  is chosen such that the obtained groups of 1 (filled states) and 0 (void states) are the most similar to each other, as they are being placed in the same group. In other words, the variation of data in either groups of 1 and 0 should be the least. Such minimization can be estimated through the combined variance  $\sigma^2$  which should depend on each classes of 1 and 0 based on their composing fractions  $\omega_1$  and  $\omega_0$ . Therefore, the global grayness threshold  $Int_c$  should be chosen as follows:<sup>55</sup>

$$\begin{aligned} &\text{Minimize } \sigma^2 \text{ Such that :} \\ &\begin{cases} \sigma^2 = \omega_0 \sigma_0^2 + \omega_1 \sigma_1^2 \\ \omega_0 + \omega_1 = 1, \end{cases} \end{aligned} \quad (5)$$

where closest is interpreted as having lowest variance.

3. The center pixel of the image, which can be approximated as the mean value of the horizontal and vertical boundary values, was taken as the initial seed. The percolation starts via connections through the first-order neighbors (left  $\leftarrow$ , right  $\rightarrow$ , top  $\uparrow$ , and bottom  $\downarrow$ ), where the region of the dendritic structure is captured progressively in consecutive steps until reaching the boundary of the microstructure, where no further progress is possible.
4. The extracted microstructure through the percolation can be extracted out from the rest of the image. As the original center was for the captured image and not necessarily the center for the microstructure, a new center is defined for the dendrite with higher precision via averaging its horizontal and vertical extents.
5. Starting from the real center as the new seed point, the percolation is re-initiated through the first-order neighbors (left  $\leftarrow$ , right  $\rightarrow$ , top  $\uparrow$ , and bottom  $\downarrow$ ) progressively in consecutive steps, where no further progress is possible. Throughout the percolation, each pixel is indexed from the higher value down to 1. Hence, the index of each pixel correlated by its percolation distance from the center seed.
6. The extent of propagation of each microstructure can be estimated from the convex hull of the filled states. Figure 3(a) illustrates an extracted microstructure through percolation, with corresponding dashed encirclement as the computed convex hull. As well, since the convex hull acts as a boundary for propagation extent, it can be used for separating the aggregation in the outer zones of the microstructure from the inner region. In this regard, Figs. 3(a) and 3(c) represent samples of outer and inner pile up in the microstructure versus during the time until the next image acquisition. In other words, we define  $\rho_O$ , representing the amount of new material added to the outer periphery between two consecutive time stamps, and  $\rho_I$  designating the same added to the interior.

From the obtained convex hull, the extent of the microstructure reach can be obtained which falls in between the inner electrode (i.e.,  $R_I = \frac{d_i}{2}$ ) and the outer electrode (i.e.,  $R_O = \frac{d_o}{2}$ ), and one has  $R_I \leq \text{Reach} \leq R_O$ . Normalizing to the outer radius  $R_O$ , one gets

$$\approx 0 < \hat{r} \leq 1,$$

where  $\hat{r}$  is the normalized reach, and the approximation sign is used since  $R_I \ll R_O$ . Mathematically, the reach  $\hat{r}$  can be calculated from the following:

$$\hat{r} = \frac{\beta}{N_{\text{CVX}} R_O} \sum \sqrt{(x_{\text{CVX},i} - x_C)^2 + (y_{\text{CVX},i} - y_C)^2}, \quad (6)$$

where  $N_{\text{CVX}}$  is the number of points in the convex hull,  $x_{\text{CVX},i}, y_{\text{CVX},i}$  are their horizontal and vertical coordinates, and  $x_C, y_C$  are the horizontal and vertical coordinates of the center of the microstructure.

Figures 4(a)–4(c) track the aforementioned density types  $\rho, \rho_O, \rho_I$  vs the scale reach  $\hat{r}$  as a measure for the progress of the dendrites, which is tracked for different electrolyte concentrations  $C_0 \in \{5, 10\}$  mM and the voltages  $V_0 \in \{3, 4, 6\}$ .

**B. Nano-density  $\rho_{\text{Nano}}$**

The nano-density  $\rho_{\text{Nano}}$  tends to estimate the structural density of growing microstructures, in lower-than-pixel scale, which cannot be captured through computational image processing.

08 June 2025 00:39:00

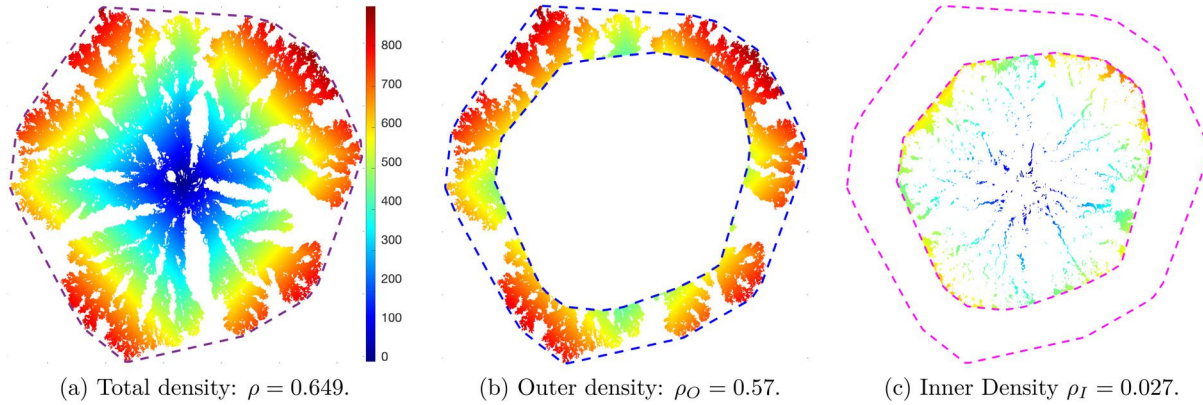


**FIG. 3.** Samples for computing the (a) total density  $\rho$ , (b) outer density  $\rho_O$ , and (c) inner density  $\rho_I$  for  $V_0 = 5$  V,  $C_0 = 10$  mM, and  $t = 200$  s. The color spectrum, from blue to red, correlates with the distance from the center.

From the percolation-based image processing in Sec. III A, one can additionally compute the rate (i.e., velocity) of propagation of the microstructures  $\hat{v}(t_k)$  as

$$\hat{v}(t_k) = \frac{\hat{r}(t_{k+1}) - \hat{r}(t_k)}{\delta t}, \quad (7)$$

where  $\delta t = t_{k+1} - t_k$ , and  $\hat{v}$  is the normalized velocity to the outer radius  $R_O$ . The trend of variation in the normalized velocity  $\hat{v}$  vs the progress of the microstructure has been explained in our prior work.<sup>46</sup> Such propagation rate is measured for the porous microstructure, which contains both material and empty sites. In fact, the existence of the empty spots exacerbates the propagation rate of the microstructure, which can be used as a handle for porosity estimation.

Herein, we establish a modeling framework for calculating the growth rate of the electrodeposited material, assuming the inherent porosity of  $\rho$ . Fundamentally, the electrochemical flux  $J$  is the confluence of the two important effects of the concentration gradient and voltage gradient, which in continuum scale can be expressed as follows:

$$J \approx -D \frac{\partial C}{\partial r} - \frac{zF}{RT} DC \frac{\partial V}{\partial r},$$

where  $D$  is the diffusivity of the ions,  $C$  is the local concentration,  $r$  is the radial distance from the center,  $z$  is the valence number of the charge carriers,  $F$  is the charge per mole ( $96.5 \text{ kC mol}^{-1}$ ),  $R$  is the gas constant ( $8.314 \text{ J mol}^{-1} \text{ K}^{-1}$ ),  $T$  is the temperature, and  $V$  is the local voltage. The first term is the diffusive flux ( $J_{DF}$ ) generated from the concentration gradient, and the second term is the electromigration flux ( $J_{MG}$ ) driven through the voltage gradient (i.e., local electric field). Meanwhile, the convective term, which the flux due to moving fluids is neglected, since the small droplet medium is static, without external stirring, the microstructures grow horizontally, it is not possible to have a gravity induced motion due to possible density gradients, and finally the droplet geometry is very thin<sup>59</sup> (Height/Diameter  $\approx 0.1$ ).

For dense electrolytes ( $C \uparrow \uparrow$ ) and lower applied voltages ( $V \downarrow \downarrow$ ), large concentration gradients can form, and one can notice ( $\frac{\partial C}{\partial r} \gg \frac{\partial V}{\partial r}$ ). In such cases, the diffusion will be the primary drive for the transport, which is known as diffusion limited aggregation (DLA).<sup>40,56</sup> Vice versa for dilute electrolytes ( $C \downarrow \downarrow$ ) and higher applied voltages ( $V \uparrow \uparrow$ ), the comparison of the gradients leads to ( $\frac{\partial C}{\partial r} \ll \frac{\partial V}{\partial r}$ ), and the electromigration term can dominate. Herein, we estimate the individual contribution of the diffusive flux ( $J_{DF}$ ) and electromigration flux ( $J_{MG}$ ) as below:

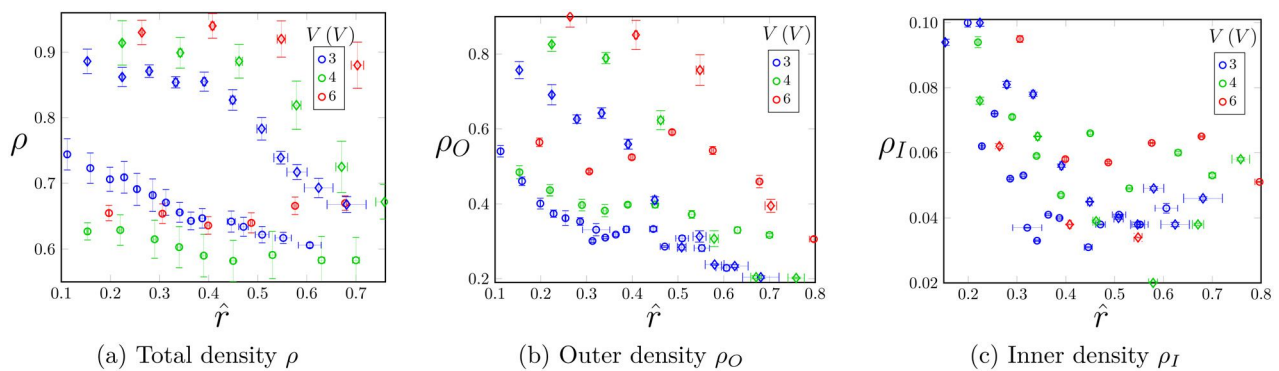


**FIG. 4.** The variations in the (a) total density  $\rho$ , (b) outer density  $\rho_O$ , and (c) inner density  $\rho_I$ , vs the normalized reach of the microstructure  $\hat{r} \in [0, 1]$  [defined in Eq. (6)], for different applied voltage values  $V_0$  (colors) and electrolyte concentrations  $C_0$  ( $\circ$ :  $C_0 = 5$  mM and  $\diamond$ :  $C_0 = 10$  mM). The error bars indicate the range of standard deviations for multiple measurements. The global  $\rho$  and outer density  $\rho_O$  measurements exhibit generally reducing trend with progress  $\hat{r}$  and larger values with higher applied voltage  $V_0$ .

$$\begin{cases} J_{DF} \sim D \frac{C_0}{\delta}, \\ J_{MG} \sim \frac{zF}{RT} DC_0 \frac{V}{\lambda}, \end{cases}$$

where  $C_0$  is the ambient molar concentration of the charge carriers in the electrolyte,  $\delta$  is the boundary layer as the gradient zone for the concentration  $C$ , and  $\lambda$  is the Debye length as the gradient zone for the electric potential  $V$ . Typically, the physical boundary is much larger than the electrical counterpart (i.e.,  $\lambda \ll \delta$ ). To simplify this comparison, we conservatively use the scale of the space charge region  $x_f$ , which falls in between these two extends ( $\lambda < x_f < \delta$ ) for both fluxes, hence over-estimating diffusion flux  $J_{DF}$  and under-estimating electromigration flux  $J_{MG}$ . In such case, the ratio of the two fluxes is simplified further as (choose  $V = 3$  V, the smallest)

$$\begin{aligned} \frac{J_{DF}}{J_{MG}} &\approx \frac{RT}{zFV} \\ &\approx \frac{8.3 \times 298}{2 \times 9.65 \times 10^4 \times 3} \\ &\approx 0.004 \ll 1 \end{aligned}$$

Therefore, for the minimum range of  $J_{MG}$  and the maximum range of  $J_{DF}$ , one still observes the dominance of the electromigration ( $J_{MG} \gg J_{DF}$ ). Hence, the upcoming ions with the drift velocity of  $v_d = \mu E$  and the sparse allocations with the concentration  $C_0$  lead to the growth of the dendritic microstructures. Considering the growing interface (dashed), the inflow of the ions ( $Cu^{2+}$ ) from solution-side, with the drift velocity  $v_d$ , will form the growing layer in the electrode-side, with the density  $\rho$ , which will grow with the speed of  $v_s$ .

In this regard, as shown in Fig. 5, the inflow of ions through the effective thickness of  $dr$  within the electrolytic of concentration  $C_0$  contains the  $n_{IN}$  number of moles as

$$n_{IN} = 2 \pi s \delta r \cdot \bar{b} \cdot C_0, \quad (8)$$

and considering  $\delta r = \mu E \delta t$ , one gets

$$n_{IN} = (2\pi \bar{b} \mu N C_0) s E \delta t, \quad (9)$$

where  $\bar{b}$  is the average in-plane thickness of the electrodeposits, and  $s$  represents the dynamic position of the growing interface. On the other hand, the number of moles in the formed solid microstructure  $n_s$  by the time span  $\delta t$  would be

$$n_s = \rho \frac{2\pi N \bar{b} s}{\Omega} v_s \delta t, \quad (10)$$

where  $\Omega$  is the molar mass of the solid copper ( $\frac{m^3}{mol}$ ),  $\rho$  is the spatial density of the accumulated microstructures ( $\frac{m^3}{m^3}$ ), and  $v_s$  is the rate of propagation in the solid microstructure. Assuming all the upcoming ions are getting deposited during the effective time interval  $dt$ , one gets

$$n_{IN} = n_s. \quad (11)$$

Hence, equating the relationships (9) and (10) and performing simplification yields the approximation for the spatial density  $\rho$  as

$$\rho = \frac{\Omega C_0}{v_s} \mu E, \quad (12)$$

where  $\mu_0$  is the electrical mobility of the upcoming ions ( $\frac{m^2}{Vs}$ ), and  $E$  is the electric field.

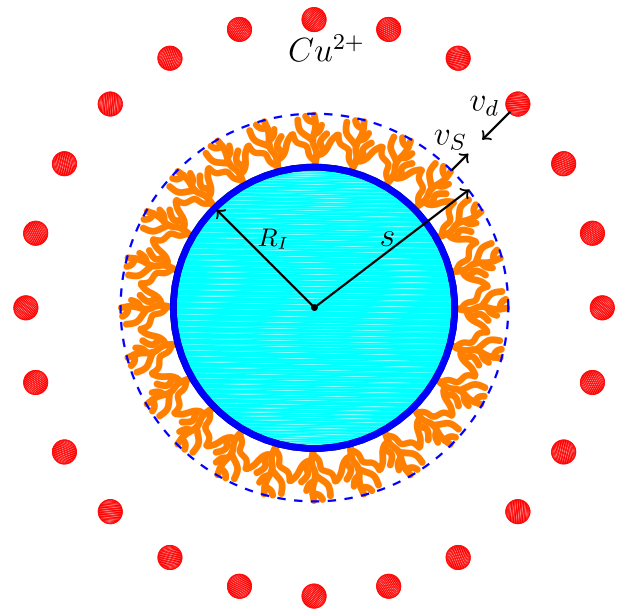


**FIG. 5.** The modeling framework for the accumulation of the upcoming ions (red) with the drift velocity  $v_d$ , forming the dendritic microstructures (orange) and the interface grows with the state and rate of  $s$  and  $\dot{s}$ .  $R_I$  is electrode radius.

Likewise, for the planar electrodeposition, one could have  $n_{IN} = w \bar{b} C_0 \mu E \delta t$  and  $n_s = \rho \frac{N \bar{b} w}{\Omega} v_s \delta t$ , where  $w$  is the width of the microstructures, and identically leads to Eq. (12).

#### IV. RESULTS AND DISCUSSION

The relationship (12) provides insights into obtaining the atomic-scale spatial density of the atoms in the amorphous/porous microstructures. In order to obtain the electric field  $E$ , the voltage profile vs the state of progress in the dendrites is obtained previously as<sup>46</sup>

$$V(r) = V_- + \left( \frac{\ln(r) - \ln(s)}{\ln(R_O) - \ln(s)} \right) \Delta V, \quad (13)$$

where  $s \leq r \leq R_O$ . Respectively, the electric field  $E$  will be solely in the radial direction, merely due to azimuthal symmetry, and will be obtained as

$$E = \left. \frac{\partial V}{\partial r} \right|_s = \frac{\Delta V}{s \ln \left( \frac{R_O}{s} \right)}. \quad (14)$$

The two correlations with the dendrite progress  $s$  in the denominator indicate such fast behavior in the initial and final stages of the propagation. Hence, there must be a minimum position in between, that is,  $s_{min}$  leading to the minimum electric field  $E_{min}$ , and it can be obtained by setting  $\frac{\partial E}{\partial s} = 0$ , which gives

$$\frac{\partial E}{\partial s} = \frac{1}{\ln(R_O) - \ln(s)} \left( \frac{1}{\ln(R_O) - \ln(s)} - 1 \right) \frac{\Delta V}{s^2} = 0,$$

which requires  $\ln \left( \frac{R_O}{s} \right) = 1$ , and one gets

$$s_{min} = \frac{R_O}{e} \approx 0.37R_O. \tag{15}$$

Hence, the electric field in  $s_{min}$  could be estimated for smallest applied voltage 3 V from Eq. (14), as below:

$$E \sim \frac{3}{0.37 \times 9 \times 10^{-3} \times \ln\left(\frac{1}{0.37}\right)} \approx 900 \frac{\text{V}}{\text{m}}.$$

Meanwhile, the electrical mobility  $\mu$  can be obtained from the Einstein relationship as

$$\begin{aligned} \mu &= \frac{Dq}{k_B T} = \frac{5.4 \times 10^{-10} \times 2 \times 1.6 \times 10^{-19}}{1.38 \times 10^{-23} \times 298} \\ &\approx 5 \times 10^{-8} \frac{\text{V}}{\text{m}^2\text{s}} \end{aligned}$$

where the diffusion coefficient  $D$  obtained for  $C_0 = 10\text{mM}$ ,<sup>57</sup> and therefore, the spatial density  $\rho$  is obtained from Eq. (12) as

$$\begin{aligned} \rho &= 7.1 \times 10^{-6} \frac{\text{m}^3}{\text{mol}} \times 10 \frac{\text{mol}}{\text{m}^3} \times \frac{5 \times 10^{-8} \times 900 \frac{\text{V}}{\text{m}}}{1.6 \times 10^{-3} \times 9 \times 10^{-3}} \\ &\approx 2.2 \times 10^{-4} \end{aligned}$$

where  $\Omega = 7.1 \times 10^{-6}$  is molar volume of copper,  $C_0 = 10\text{mM}$ , and  $v_S \approx 1.6 \times 10^{-3}\text{m/s}$  is the average progress rate of the microstructures estimated from Eq. (7).<sup>46</sup>

From averaging the micro-density values in Fig. 4(a), one can approximate  $\rho_{\text{Micro}} \approx 0.75$ , and the range of the remainder density in nano (i.e., atomic) scale will be obtained from Eq. (3) as

$$\rho_{\text{Nano}} \in [10^{-4}, 10^{-3}]. \tag{16}$$

As well, the original linear correlation assumption of the drift velocity  $v_d$  and the electric field ( $v_d = \mu E$ ), which signifies the domination of the electromigration, can be verified from the experimental measurements of the prior work,<sup>46</sup> where both the propagation front velocity  $v_S$  and the electric field  $E$  have similar fast–slow–fast behavior throughout the growth life of the propagation front. In other words, the initial acceleration of the microstructures is due to smaller real-estate for the radius of curvature in the growing interface (curvature effect of the electrode), whereas the later stage acceleration behavior is due to enhanced electric field toward the end. This suggests that both the velocity of dendrites  $v_S$  and the electric field  $E$  experience a version of fast–slow–fast behavior.

Regarding the effective factors leading to the density of the microstructures, one could categorize them as the charging condition (i.e.,  $V_0$ ), the involved solution (i.e.,  $C_0$ ), as well as the interface geometry ( $\hat{r}$ ), where each factor could become dominant if others have minor contribution. In general, one could observe that the total  $\rho$  and outer  $\rho_O$  solid density is reduced throughout the growth life, till short-circuiting almost in all cases. Regarding the inner density  $\rho_I$ , a noticeable trend was not observed, and its value is considerable smaller than the total  $\rho$  and outer density  $\rho_O$ . Herein, we explore the contribution of each factor individually, as below:

### A. Applied voltage $V_0$

The voltage profile vs the normalized distance  $\hat{r}$  would yield initially reducing ( $E \downarrow$ ) and later-on increasing ( $E \uparrow$ ) behavior for the

electric field, with the minimum value as obtained in Eq. (15). Hence, the voltage would not mainly be effective during the initial growth. Since, the electric field  $E$  acts in favor of dendritic development (less solid density). Therefore, the role of the voltage becomes more pronounced toward the end of growth life of the microstructures, where the high electric field forms more dendritic (directed) growth of the branches and the density is reduced.

### B. Solution concentration $C_0$

One could ascribe that the higher molar concentration ( $C_0 \uparrow$ ) of the electrolyte would yield more availability of the ions, better aggregation, and more packed formation of the microstructures, which is obvious for all computations of the total and outer densities  $\rho, \rho_O$  in 10 mM compared to 5 mM. This shows that the electrolyte concentration is a highly effective parameter, in the range considered.

### C. Geometry $\hat{r}$

The role of geometry could be considered from the perspective of electrodeposition area  $A$  and curvature  $\kappa$  of the growing front. Initially, the propagating microstructure has smallest area ( $A \downarrow\downarrow$ ) and largest curvature ( $\kappa \uparrow\uparrow$ ). As the microstructures evolve, the area increases ( $A \uparrow$ ), and the curvature is reduced ( $\kappa \downarrow$ ). Area-wise, the increase in the real-estate for electrodeposition means more sparse and directed growth, ( $\rho \downarrow$ ), while curvature-wise, initially the convex interface makes the growing branches diverge from each other with the higher rate, whereas later-on the growing interface gets flattened, and the diverging rate is reduced and the electrodeposition should get more packed ( $\rho \uparrow$ ). During such competition, the overall reducing trend in the density values  $\rho, \rho_O$  signifies the dominance in the effect of area, than the curvature. As well, such geometry-induced reduction in the density values  $\rho$  and  $\rho_O$  is more pronounced [i.e., sharper slopes in Figs. 4(a) and 4(b)] when other factors are less in magnitude, such as lower applied voltage.

Summarizing the effect of the aforementioned factors in the solid density, one can ascribe the below definitive methods to increase the electrodeposition density  $\rho$ , while other factors are subjected to more detailed investigation,

$$C_0 \uparrow, \quad \kappa \downarrow \Rightarrow \rho \uparrow.$$

As well, one should note that due to fast electrodeposition, the glass-style, metastable, and non-equilibrium formation of the microstructures is kinetics-dominated process, which is merely a random allocation and not necessarily leads to the energy-minimized microstructure.

One could additionally investigate the effect of the selected method for thresholding/binarization in the computed densities. While in general the mentioned method should vary, in this study there have minimal effect on the obtained density value, due to discernible contrast between the solid and void parts as well as not possessing a considerable gray zone. The two widely different methods of generalized Otsu (global) and adaptive thresholding (local) are compared visually in Fig. 6, where  $Int_c$  is the global threshold value, and  $\overline{Int}_c$  is the average of all threshold values optimized in local scale. The relative error Err could be quantified via computing the difference between the obtained global  $\rho_{\text{Global}}$  and local  $\rho_{\text{Local}}$  methods, as

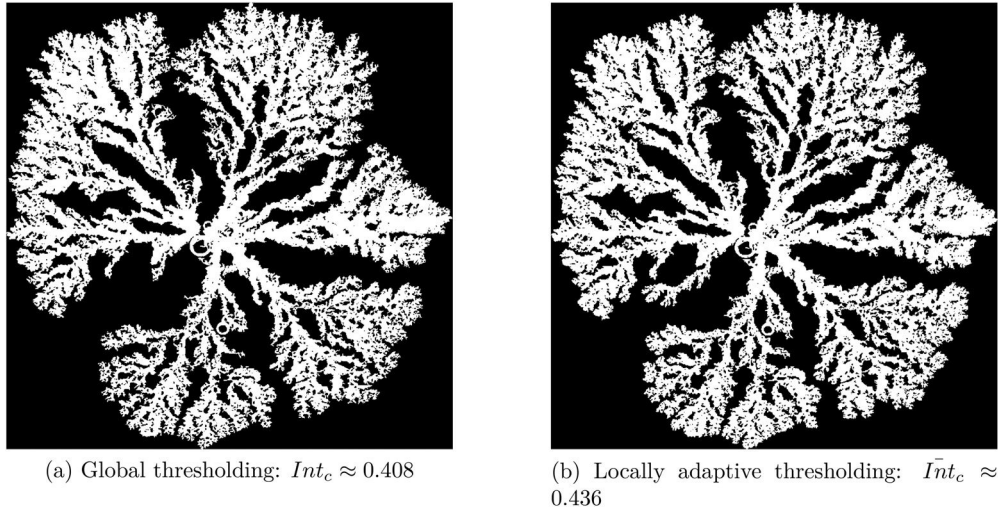


FIG. 6. The comparison between the binarization methods: (a) global thresholding and (b) local adaptive thresholding.

$$\text{Err} = \frac{\rho_{\text{Global}} - \rho_{\text{Local}}}{\rho_{\text{Global}}} \approx 5\%,$$

$$D_f = -\frac{\log N}{\log \varepsilon}. \tag{17}$$

which is the difference obtained for two highly distinct methods. In this regard, choosing a consistent thresholding method ensures the accuracy of the obtained density trends, due to equal treatments.

Another aspect describing the complexity of the grown morphology is the fractal dimension  $D_f$ , which is defined as

$$N = \varepsilon^{-D_f},$$

where  $N$  is the number of filled states (i.e., material), and  $\varepsilon$  is the dimension. In other words, the fractal dimension can be obtained from the following:

As an example, in previous works, the fractal dimension in the voltage range (between 7 and 8 V) has been identified to have the minimum value.<sup>44</sup> Herein, we evaluate the transient variation of  $D_f$  and observe a distinct zigzag trend constituting several peaks and troughs, while the microstructure propagates toward the outer electrode. This inherently indicates that the structural features vary with time which can be directly correlated with its position inside the inter-electrode space. Such wavy pattern in  $D_f$  can be explained in terms of the oscillating between the nucleation and the branching described in the past.<sup>37</sup> In fact, the sewing of the dendritic front is

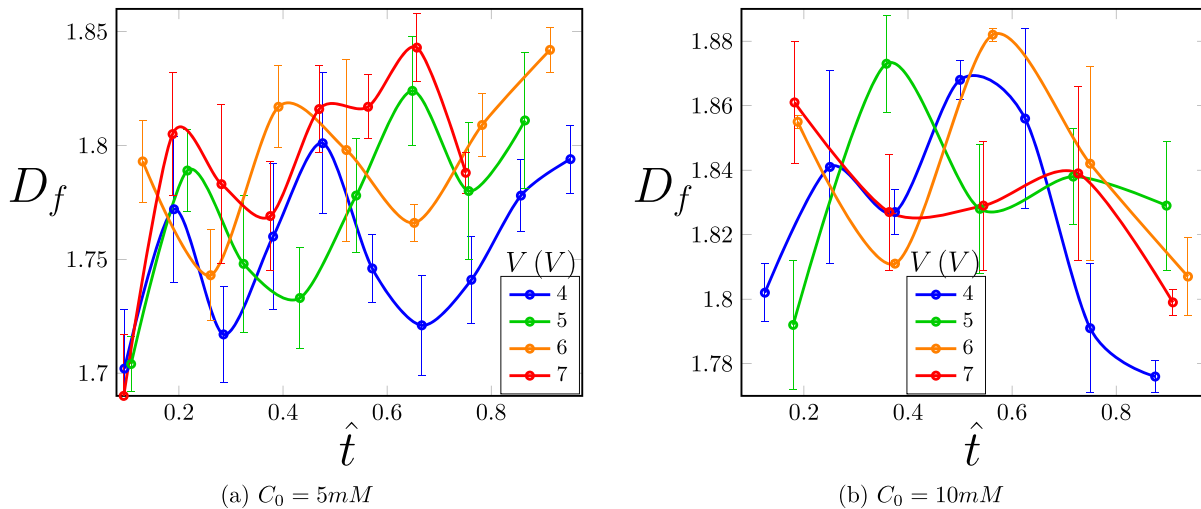


FIG. 7. Identification of oscillatory behavior in the fractal dimension which infers nucleation ( $D_f \uparrow$ ) vs branching ( $D_f \downarrow$ ) during the growth of the microstructures. (a)  $C_0 = 5 \text{ mM}$  and (b)  $C_0 = 10 \text{ mM}$ .

the result of a balanced dynamics between direct extension of a main branch and lateral nucleations of its sub-branches on its body. The more a branch grows, the more it achieves peripheral area, where the nucleation of new sub-branch becomes progressively higher (more surface area  $\sim$  more nucleation possibility). When reaching a critical arm length, a new sub-branch is initiated. Such direct-lateral growth dynamics generate highly porous microstructure in batteries with excessive surface-to-volume ratio, which is metastable and thermally unstable, can dissociate during prolonged cycles, and reduce the charge capacity, particularly in higher temperatures.<sup>58,59</sup>

Regarding the branching phase, as the tip grows, its velocity is chronologically decreased until it becomes much smaller than the anionic recession speed, because the average growth speed of the tip is the same as the anionic speed. With time, the space charge is again recovered, and the surface field tends to overcome the critical value to generate a new nucleation event.

A closer look into computing the fractal dimension in Eq. (17) indicates that this version of the fractal dimension correlates with the density  $\rho$  of the microstructures since it is a measure of filled states over the dimension. Therefore, for the zigzag pattern provided in Fig. 7, the increasing trends toward the peaks indicate the nucleation (i.e., filling), whereas the decreasing trend toward the minima signifies the branching (i.e., extending porous arms).

## V. CONCLUSIONS

In this paper, the density dendritic microstructures have been explored in the circular domain, both by means of experimental observation followed by image processing, as well as theoretical modeling. Initially, the evolution pattern of the microstructures is analyzed via developing a percolation-based image processing protocol to quantify the formed voids in between the growing branches. The solid-mass density has been observed to reduce almost in all cases during the growth life, till short-circuiting, which is correlated with increasing interfacial radius of curvature and hence the deposition real-estate, as well as increased electric field, which enhances more direct (i.e., faster) and less lateral formation of the branches. In parallel, an analytical model has been developed to evaluate the solid nano-density  $\rho_{\text{Nano}}$  of the growing microstructure. Comparing the velocity outcomes of the growth front in the experiments—with invisible emptiness inside the visible solid mass—and atomic-scale modeling, we have estimated an extent for the nano-scale density  $\rho_{\text{Nano}} \sim [10^{-4}, 10^{-3}]$  of the growing microstructures. Consequently, the fractal dimension  $D_f$  was tracked during the growth life where its zigzag behavior was correlated with the oscillatory behavior between nucleation of new seed branches and extension of existing ones. The results could be useful for comprehending on the atomic-scale density  $\rho_{\text{Nano}}$  of the microstructures, which is beyond the reach of microscopic measurements, as well as understanding the variation in the local structural density in circular growth of the dendritic microstructures.

## SUPPLEMENTARY MATERIAL

See the [supplementary material](#) for the raw data from the real-time experimental measurements and the scripts for processing of the images, computations of the total, outer, and inner densities, their interpolations, and finally estimating the real-time fractal dimensions.

## ACKNOWLEDGMENTS

The authors gratefully acknowledge the financial support from the Indian Institute of Technology Kharagpur (Sanction Letter No. IIT/SRIC/ATDC/CEM/2013 – 14/118, dated 19.12.2013).

## AUTHOR DECLARATIONS

### Conflict of Interest

The authors have no conflicts to disclose.

### Author Contributions

Asghar Aryanfar and Trina Dhara contributed equally to this work.

**Asghar Aryanfar:** Conceptualization (equal); Data curation (equal); Formal analysis (equal); Software (equal); Validation (equal); Visualization (equal); Writing – original draft (equal); Writing – review & editing (equal). **Trina Dhara:** Conceptualization (equal); Writing – original draft (equal); Writing – review & editing (equal). **Sunando DasGupta:** Project administration (equal); Supervision (equal).

## DATA AVAILABILITY

The data that support the findings of this study are available from the corresponding author upon reasonable request.

## NOMENCLATURE

$\bar{b}$	Ave. thickness of electrodeposits (m)
$C$	Local ionic concentration ( $\text{mol m}^{-3}$ )
$C_0$	Bulk electrolyte concentration (M)
$D$	Bulk diff. coefficient ( $\text{m}^2 \text{s}^{-1}$ )
$D_f$	Fractal dimension
$d_I/R_I$	Dia./radius of the cathode (m)
$d_O/R_O$	Dia./radius of the circular anode (m)
$E$	Electric field ( $\text{V/m}^{-1}$ )
$F$	Faraday's constant ( $\text{C mol}^{-1}$ )
$f_R, f_G, f_B$	Red/green/blue coefficients ([ ])
$Int/Int_c$	Intensity/critical intensity value
$i_0$	Exchange current density ( $\text{A m}^{-2}$ )
$J$	Total ionic flux ( $\text{mol m}^2 \text{s}^{-1}$ )
$J_{DF}/J_{MG}$	Diffusive/electromigration flux
$k_B$	Boltzmann constant ( $\text{J K}^{-1}$ )
$N$	Avogadro number (mol)
$N$	Number of filled states by the boxes
$N_{CVX}$	Number of points/convex
$n_{IN}$	Number of moles of upcoming ions in $\delta r$
$n_S$	Number of atoms composing $\delta s$
$q$	Charge per volume ( $\text{C m}^{-3}$ )
$\hat{r}$	Normalized reach
$s$	Position of the growing interface (m)
$s_{min}$	Position of minimum voltage (m)
$t_k$	Times in the step $k$
$V(r)$	Voltage at position $r$ (V)
$V_-$	Cathodic potential (V)
$V_0$	Applied voltage (V)
$v_d$	Ionic drift velocity ( $\text{m s}^{-1}$ )

$v_S$	Rate of solid propagation ( $\text{ms}^{-1}$ )
$\hat{v}(t_k)$	Normalized front velocity at time $t_k$ ( $\text{s}^{-1}$ )
$x, y$	Horizontal/vertical coordinates
$x_C, y_C$	Horizontal/vertical coords of center
$x_{CVX}$	Horizontal coords/convex hull
$x_I$	Thickness of the space charge layer (m)
$y_{CVX}$	Vertical coord/convex hull
$z$	Valence number
$\beta$	Calibration factor ( $\text{mm pixel}^{-1}$ )
$\Delta V$	Applied voltage difference (V)
$\varepsilon$	Dimension
$\mu_0$	Ionic mobility ( $\text{m}^2 \text{V}^{-1} \text{s}^{-1}$ )
$\rho$	$\rho_{\text{Micro}}/\rho_{\text{Nano}}$ Total/micro/nano density
$\rho_O/\rho_I$	Outer/inner density
$\sigma^2, \sigma_0^2, \sigma_1^2$	Total/white/black pixels variance
$\omega_0, \omega_1$	Fractions of white/black portions
$\Omega$	Molar mass of copper ( $\text{m}^3 \text{mol}^{-1}$ )

## APPENDIX: KELVIN EFFECT

One other aspect of the branches is the radius of the curvature  $r$  of the propagation front, which would increase the required overpotential for electrodeposition. Hence, the total overpotential  $\eta$  becomes

$$\eta = \frac{i RT}{i_0 F} + \frac{irRT}{DC_0F^2} + \frac{2\gamma V}{Fr}, \quad (\text{A1})$$

where  $i$  is the applied current density,  $i_0$  is the exchange current density in equilibrium,  $R$  is gas constant,  $T$  is the temperature,  $F$  is Faraday's constant,  $r$  is radius of curvature,  $D$  is diffusion coefficient,  $C_0$  is ambient electrolyte concentration, and  $V$  is molar volume. Obviously, the surface energy  $\gamma$  becomes the most effective when the radius of curvature  $r$  is very small. Herein, we calculate each term separately, considering the smallest formed tip radius on the order of  $\sim 10$  atoms, for analogy:

The current density  $i$  varies roughly between  $\sim 1$  and  $\sim 10 \text{ mAcm}^{-2}$ , and here we assume the average value of  $5 \text{ mAcm}^{-2}$ . The closest exchange current density  $i_0$  is found to be  $11 \text{ A m}^{-2}$ ,<sup>60</sup> the surface energy is averaged for a range of the solvent concentration as  $2.5 \times 10^4 \text{ J m}^{-2}$ ,<sup>61</sup> and the radius of curvature would be

$$\begin{aligned} r &\approx 10 \times 1.28 \times 10^{-10} \\ &= 1.28 \times 10^{-9} \end{aligned}$$

and the individual overpotential terms are computed as

$$\left\{ \begin{aligned} \frac{i RT}{i_0 F} &\sim \frac{50}{11} \times \frac{8.3 \times 298}{96500} \approx 0.12 \\ \frac{irRT}{DC_0F^2} &\sim \frac{5 \times 10^{-3} \times 1.28 \times 10^{-9} \times 8.3 \times 298}{2\pi(4.5 \times 10^{-3}) \times 30 \times 10^{-6} \times 10 \times 10^{-3}} = 1.87 \\ \frac{2\gamma V}{Fr} &= \frac{2 \times 2.5 \times 10^4 \times 7.1 \times 10^{-6}}{96500 \times 1.28 \times 10^{-9}} = 2.87 \times 10^{-5}, \end{aligned} \right.$$

which proves that the Kelvin effect in this system could be neglected.

## REFERENCES

- P. Augustyn, P. Rytlewski, K. Moraczewski, and A. Mazurkiewicz, "A review on the direct electroplating of polymeric materials," *J. Mater. Sci.* **56**(27), 14881–14899 (2021).
- A. P. Abbott, G. Frisch, and K. S. Ryder, "Electroplating using ionic liquids," *Annu. Rev. Mater. Res.* **43**(1), 335–358 (2013).
- I. Gurrappa and L. Binder, "Electrodeposition of nanostructured coatings and their characterization—A review," *Sci. Technol. Adv. Mater.* **9**, 043001 (2008).
- F. C. Walsh, S. Wang, and N. Zhou, "The electrodeposition of composite coatings: Diversity, applications and challenges," *Curr. Opin. Electrochem.* **20**, 8–19 (2020).
- J. Pu, Z. Shen, C. Zhong, Q. Zhou, J. Liu, J. Zhu, and H. Zhang, "Electrodeposition technologies for Li-based batteries: New frontiers of energy storage," *Adv. Mater.* **32**(27), 1903808 (2020).
- M. Bernal Lopez and J. Ustarroz, "Electrodeposition of nanostructured catalysts for electrochemical energy conversion: Current trends and innovative strategies," *Curr. Opin. Electrochem.* **27**, 100688 (2021).
- E. Shalyt, M. Pavlov, and C. Bai, "Green electrodeposition trends in semiconductor industry," *ECS Trans.* **53**(19), 1 (2013).
- G. Crabtree, E. Kócs, and L. Trahey, "The energy-storage frontier: Lithium-ion batteries and beyond," *MRS Bull.* **40**(12), 1067–1078 (2015).
- X.-B. Cheng, R. Zhang, C.-Z. Zhao, and Q. Zhang, "Toward safe lithium metal anode in rechargeable batteries: A review," *Chem. Rev.* **117**(15), 10403–10473 (2017).
- G. Liang, F. Mo, Q. Yang, Z. Huang, X. Li, D. Wang, Z. Liu, H. Li, Q. Zhang, and C. Zhi, "Commencing an acidic battery based on a copper anode with ultrafast proton-regulated kinetics and superior dendrite-free property," *Adv. Mater.* **31**(52), 1905873 (2019).
- Q. Wang, B. Liu, Y. Shen, J. Wu, Z. Zhao, C. Zhong, and W. Hu, "Confronting the challenges in lithium anodes for lithium metal batteries," *Adv. Sci.* **8**(17), 2101111 (2021).
- X. Zhang, A. Wang, X. Liu, and J. Luo, "Dendrites in lithium metal anodes: Suppression, regulation, and elimination," *Acc. Chem. Res.* **52**(11), 3223–3232 (2019).
- M. K. Aslam, Y. Niu, T. Hussain, H. Tabassum, W. Tang, M. Xu, and R. Ahuja, "How to avoid dendrite formation in metal batteries: Innovative strategies for dendrite suppression," *Nano Energy* **86**, 106142 (2021).
- X. Ke, Y. Wang, L. Dai, and C. Yuan, "Cell failures of all-solid-state lithium metal batteries with inorganic solid electrolytes: Lithium dendrites," *Energy Storage Mater.* **33**, 309–328 (2020).
- K.-H. Chen, K. N. Wood, E. Kazyak, W. S. LePage, A. L. Davis, A. J. Sanchez, and N. P. Dasgupta, "Dead lithium: Mass transport effects on voltage, capacity, and failure of lithium metal anodes," *J. Mater. Chem. A* **5**(23), 11671–11681 (2017).
- F. Ding, W. Xu, G. L. Graff, J. Zhang, M. L. Sushko, X. Chen, Y. Shao, M. H. Engelhard, Z. Nie, and J. Xiao, "Dendrite-free lithium deposition via self-healing electrostatic shield mechanism," *J. Am. Chem. Soc.* **135**(11), 4450–4456 (2013).
- H. Wan, J. Xu, and C. Wang, "Designing electrolytes and interphases for high-energy lithium batteries," *Nat. Rev. Chem.* **8**(1), 30–44 (2023).
- Z. Liu, M. S. Islam, Y. Fang, M. Zhu, C. C. Cao, and G. Xu, "Design strategies and performance enhancements of PVDF-based flexible electrolytes for high-performance all-solid state lithium metal batteries," *Nanoscale* **17**, 2408–2422 (2025).
- M. Wu, Y. Liu, Z. Zhang, Y. Wang, H. He, H. Zhu, K. Xu, J. Wang, and J. Lu, "Fabrication of sustainable anti-icing metal surface with micro-nano composite concave angle structure by laser-electrodeposition-chemical method," *Surf. Coat. Technol.* **483**, 130820 (2024).
- P. Molaiyan, M. Abdollahifar, B. Boz, A. Beutl, M. Krammer, N. Zhang, A. Tron, M. Romio, M. Ricci, R. Adelung *et al.*, "Optimizing current collector interfaces for efficient anode free lithium metal batteries," *Adv. Funct. Mater.* **34**(6), 2311301 (2024).
- K. Eiler, F. Alcaide, E. García-Lecina, J. Sort, and E. Pellicer, "Mesoporous Ni-Pt nanoparticles on Ni foam by electrodeposition: Dual porosity for efficient alkaline hydrogen evolution," *Int. J. Hydrogen Energy* **99**, 448–457 (2025).
- D. B. Bailmare, B. V. Malozymov, and A. D. Deshmukh, "Electrodeposition of porous metal-organic frameworks for efficient charge storage," *Commun. Chem.* **7**(1), 178 (2024).

- <sup>23</sup>M. Lee, J. Won, H. Shin, J. Lee, M. H. Lee, and S. Oh, "Porous Ni-Fe-Cr electrocatalyst for the oxygen and hydrogen evolution reaction via facile one-step electrodeposition," *Int. J. Hydrogen Energy* **51**, 536–544 (2024).
- <sup>24</sup>P. Ji, W. Chen, Y. Luo, Y. Wang, N. Gu, G. Meng, J. Wu, B. Li, K. Wu, and Z. Liu, "3D porous mxene induced by zinc-assisted electrodeposition for flexible all-solid-state supercapacitors," *J. Alloys Compd.* **997**, 174426 (2024).
- <sup>25</sup>T. Dhara, A. Aryanfar, A. Ghosh, U. Ghosh, P. Mukherjee, and S. DasGupta, "The role of pulse duty cycle and frequency on dendritic compression," *J. Phys. Chem. C* **127**(9), 4407–4415 (2023).
- <sup>26</sup>A. Aryanfar, D. Brooks, B. V. Merinov, W. A. Goddard III, A. J. Colussi, and M. R. Hoffmann, "Dynamics of lithium dendrite growth and inhibition: Pulse charging experiments and Monte Carlo calculations," *J. Phys. Chem. Lett.* **5**(10), 1721–1726 (2014).
- <sup>27</sup>A. Ibanez and E. Fatas, "Mechanical and structural properties of electrodeposited copper and their relation with the electrodeposition parameters," *Surf. Coat. Technol.* **191**(1), 7–16 (2005).
- <sup>28</sup>A. Aryanfar, Y. Ghamlouche, and W. A. Goddard III, "Optimization of charge curve for the extreme inhibition of growing microstructures during electrodeposition," *MRS Bull.* **47**(7), 665–674 (2022).
- <sup>29</sup>Y. Liu, M. Wu, Z. Zhang, Y. Wang, L. Meng, K. Cai, H. Zhu, K. Xu, and J. Lu, "Preparation of multifunctional protective coating on alloy surface by laser-electrodeposition additive-subtractive hybrid manufacturing," *J. Mater. Process. Technol.* **326**, 118340 (2024).
- <sup>30</sup>Y. Liu, M. Wu, Z. Zhang, K. Luo, J. Lu, L. Lin, K. Xu, H. Zhu, B. Wang, W. Lei *et al.*, "Fabrication of wear-resistant and superhydrophobic aluminum alloy surface by laser-chemical hybrid methods," *Phys. Fluids* **35**(5), 052108 (2023).
- <sup>31</sup>A. S. J. Alujjage, B. S. Vishnugopi, A. Karmakar, D. P. Magee, Y. Barsukov, and P. P. Mukherjee, "Internal temperature evolution metrology and analytics in Li-ion cells," *Adv. Funct. Mater.* (published online 2025).
- <sup>32</sup>D. Ren, H. Hsu, R. Li, X. Feng, D. Guo, X. Han, L. Lu, X. He, S. Gao, J. Hou *et al.*, "A comparative investigation of aging effects on thermal runaway behavior of lithium-ion batteries," *eTransportation* **2**, 100034 (2019).
- <sup>33</sup>S. Wu, C. Wang, W. Luan, Y. Zhang, Y. Chen, and H. Chen, "Thermal runaway behaviors of Li-ion batteries after low temperature aging: Experimental study and predictive modeling," *J. Energy Storage* **66**, 107451 (2023).
- <sup>34</sup>A. Aryanfar, D. J. Brooks, A. J. Colussi, B. V. Merinov, W. A. Goddard III, and M. R. Hoffmann, "Thermal relaxation of lithium dendrites," *Phys. Chem. Chem. Phys.* **17**(12), 8000–8005 (2015).
- <sup>35</sup>Y. Troxler, B. Wu, M. Marinescu, V. Yufit, Y. Patel, A. J. Marquis, N. P. Brandon, and G. J. Offer, "The effect of thermal gradients on the performance of lithium-ion batteries," *J. Power Sources* **247**, 1018–1025 (2014).
- <sup>36</sup>R. Carter and C. T. Love, "Modulation of lithium plating in li-ion batteries with external thermal gradient," *ACS Appl. Mater. Interfaces* **10**(31), 26328–26334 (2018).
- <sup>37</sup>V. Fleury, "Branched fractal patterns in non-equilibrium electrochemical deposition from oscillatory nucleation and growth," *Nature* **390**(6656), 145–148 (1997).
- <sup>38</sup>C.-P. Chen and J. Jorné, "Fractal analysis of zinc electrodeposition," *J. Electrochem. Soc.* **137**(7), 2047 (1990).
- <sup>39</sup>J. N. Chazalviel, "Electrochemical aspects of the generation of ramified metallic electrodeposits," *Phys. Rev. A* **42**(12), 7355–7367 (1990).
- <sup>40</sup>T. A. Witten and L. M. Sander, "Diffusion-limited aggregation," *Phys. Rev. B* **27**(9), 5686 (1983).
- <sup>41</sup>R. Akolkar, "Mathematical model of the dendritic growth during lithium electrodeposition," *J. Power Sources* **232**, 23–28 (2013).
- <sup>42</sup>D. Barkey, P. Garik, E. Ben-Jacob, B. Miller, and B. Orr, "Growth velocity, the limiting current, and morphology selection in electrodeposition of branched aggregates," *J. Electrochem. Soc.* **139**(4), 1044 (1992).
- <sup>43</sup>D. B. Hibbert and J. R. Melrose, "Electrodeposition in support: Concentration gradients, an ohmic model and the genesis of branching fractals," *Proc. R. Soc. London, Ser. A* **423**(1864), 149–158 (1989).
- <sup>44</sup>N. M. Santos and D. M. F. Santos, "A fractal dimension minimum in electrodeposited copper dendritic patterns," *Chaos, Solitons Fractals* **116**, 381–385 (2018).
- <sup>45</sup>A. Aryanfar, A. Tayyar, and W. A. Goddard III, "Dendritic propagation on circular electrodes: The impact of curvature on the packing density," *Phys. Rev. E* **108**(1), 014801 (2023).
- <sup>46</sup>A. Aryanfar, T. Dhara, and S. DasGupta, "Dynamics of electrochemical dendritic propagation in circular domains," *Phys. Fluids* **37**(1), 013347 (2025).
- <sup>47</sup>M. Qiu, G. D. Finlayson, and G. Qiu, "Contrast maximizing and brightness preserving color to grayscale image conversion," in Proceedings of the 4th European Conference on Colour in Graphics, Imaging, and Vision (CGIV 2008)/10th International Symposium on Multispectral Colour Science IS&T/MCS'08, 2008, pp. 347–351.
- <sup>48</sup>R. Guo and S. M. Pandit, "Automatic threshold selection based on histogram modes and a discriminant criterion," *Mach. Vision Appl.* **10**, 331–338 (1998).
- <sup>49</sup>C. V. Jawahar, P. K. Biswas, and A. K. Ray, "Investigations on fuzzy thresholding based on fuzzy clustering," *Pattern Recognit.* **30**(10), 1605–1613 (1997).
- <sup>50</sup>H.-D. Cheng, Y.-H. Chen, and Y. Sun, "A novel fuzzy entropy approach to image enhancement and thresholding," *Signal Process.* **75**(3), 277–301 (1999).
- <sup>51</sup>C.-K. Leung and F. K. Lam, "Maximum segmented image information thresholding," *Graphical Models Image Process.* **60**(1), 57–76 (1998).
- <sup>52</sup>J. Sauvola and M. Pietikäinen, "Adaptive document image binarization," *Pattern Recognit.* **33**(2), 225–236 (2000).
- <sup>53</sup>N. Otsu, "A threshold selection method from gray-level histograms," *Automatica* **11**(285–296), 23–27 (1975).
- <sup>54</sup>A. Aryanfar, M. R. Hoffmann, and W. A. Goddard III, "Finite-pulse waves for efficient suppression of evolving mesoscale dendrites in rechargeable batteries," *Phys. Rev. E* **100**(4), 042801 (2019).
- <sup>55</sup>D. Bradley and G. Roth, "Adaptive thresholding using the integral image," *J. Graphics Tools* **12**(2), 13–21 (2007).
- <sup>56</sup>V. Sidoravicius and A. Stauffer, "Multi-particle diffusion limited aggregation," *Invent. Math.* **218**(2), 491–571 (2019).
- <sup>57</sup>R. A. Noulty and D. G. Leaist, "Diffusion in aqueous copper sulfate and copper sulfate-sulfuric acid solutions," *J. Solution Chem.* **16**(10), 813–825 (1987).
- <sup>58</sup>S. Abada, M. Petit, A. Lecocq, G. Marlair, V. Sauvart-Moynot, and F. Huët, "Combined experimental and modeling approaches of the thermal runaway of fresh and aged lithium-ion batteries," *J. Power Sources* **399**, 264–273 (2018).
- <sup>59</sup>V. Kabra, A. Karmakar, B. S. Vishnugopi, and P. P. Mukherjee, "Quantifying the effect of degradation modes on Li-ion battery thermal instability and safety," *Energy Storage Mater.* **74**, 103878 (2025).
- <sup>60</sup>J. T. Hinatsu and F. R. Foulkes, "Electrochemical kinetic parameters for the cathodic deposition of copper from dilute aqueous acid sulfate solutions," *Can. J. Chem. Eng.* **69**(2), 571–577 (1991).
- <sup>61</sup>K. I. Popov, N. D. Nikolic, and Z. Lj Rakočević, "The estimation of solid copper surface tension in copper sulfate solutions," *J. Serb. Chem. Soc.* **67**(11), 769–775 (2002).